RSC Advances

PAPER

View Article Online
View Journal | View Issue

Cite this: *RSC Adv.*, 2021, **11**, 36782

Oxygen-enriched surface modification for improving the dispersion of iron oxide on a porous carbon surface and its application as carbon molecular sieves (CMS) for CO_2/CH_4 separation

Nur Indah Fajar Mukti,[abc] Teguh Ariyanto,[ac] Wahyudi Budi Sediawan[a] and Imam Prasetyo *[ac]

The separation of CO_2/CH_4 can be enhanced by impregnating porous carbon with iron oxide. Dispersion of iron oxide is one of the critical factors which supports the separation process performance. Iron oxide dispersion can be enhanced by enriching the oxygen functional groups on the carbon surface. This study investigates three distinct oxidation processes: oxidation with a 10% H_2O_2 solution, ozonation with distilled water, and ozonation with a 10% H_2O_2 solution. The research steps included the following: (i) oxidation, (ii) impregnation of iron oxide followed by calcination, (iii) material characterization, and (iv) material performance analysis. Materials were characterized using N_2 sorption analysis, X-ray diffraction analysis (XRD), scanning electron microscopy-energy dispersive X-ray spectroscopy analysis (SEM-EDX), and Fourier transform infrared analysis (FT-IR). Iron oxide was well dispersed on the carbon surface, as evidenced by the elemental mapping of materials. In addition, the oxygen functional groups increased significantly in the range of 28.6–79.7% following the oxidation process, as indicated by the elemental component using SEM-EDX analysis. The impregnation of iron oxide on oxidized carbon ozonated with distilled water (COA–Fe) obtained a maximum CO_2 uptake capacity of 3.0 mmol g^{-1} and CO_2/CH_4 selectivity increased by up to 190% at a temperature of 30 °C and pressure of 1 atm. Furthermore, the enhancement of CO_2/CH_4 separation up to 1.45 times was the best performance achieved by COA–Fe. Thus, improving iron oxide dispersion on oxidized carbon surfaces has a potential application in CO_2/CH_4 separation.

Received 9th October 2021
Accepted 10th November 2021

DOI: 10.1039/d1ra07481d

rsc.li/rsc-advances

1 Introduction

Biogas is a renewable energy source that can be substituted for fossil fuels and natural gas. A typical biogas mixture contains 50–70% CH_4 and 30–49% CO_2.[1,2] Carbon dioxide removal from CO_2/CH_4 gas mixtures is critical since it results in a more energy-dense product, due to the high calorific value of methane. In contrast, carbon dioxide has no heating value.[3] A number of technologies are currently available to remove carbon dioxide, including absorption, membrane separation, and cryogenic separation.[4,5] However, these technologies are energy-intensive and costly. Adsorption-based separation is considered promising for CO_2/CH_4 separation because it produces high-purity methane (>98 percent vol), is relatively inexpensive, easy to operate, and energy-efficient.[6] Adsorption-based separation occurs due to the difference in affinity and diffusivity of CO_2 and CH_4.[7] Several types of molecular sieves, including zeolite molecular sieve (ZMS),[8,9] carbon molecular sieve (CMS),[10–13] and metal–organic framework (MOF),[14,15] are widely used for adsorption-based separation. Molecular sieves made from carbon are relatively stable long-term due to the low heat of adsorption and can be synthesized from a variety of materials, including coal,[16,17] biomass,[10,18] and polymer.[12,19] As a consequence, it is simple to regenerate.

CMS material derived from palm kernel shells (PKS) was investigated for CO_2/CH_4 separation. This material achieved separation ratios of up to 2.[10] However, the adsorption capacity of CO_2 is quite limited, which will require further investigation. Metal oxide impregnation may enhance carbon dioxide uptake.[20] In contrast, metal oxide agglomerations are common due to the fact that carbon is non-polar and hydrophobic, whereas metals are polar and hydrophilic. To enhance dispersion, reduced metal oxide agglomeration is employed. In recent years, several authors have discussed the use of highly dispersed iron oxide for a wide variety of applications.[21–23]

[a]*Department of Chemical Engineering, Faculty of Engineering, Universitas Gadjah Mada, Yogyakarta, 55281, Indonesia. E-mail: imampras@ugm.ac.id*

[b]*Department of Chemical Engineering, Faculty of Industrial Technology, Universitas Islam Indonesia, Yogyakarta, 55584, Indonesia*

[c]*Carbon Material Research Group, Department of Chemical Engineering, Universitas Gadjah Mada, Yogyakarta, 55281, Indonesia*

The addition of oxygen groups to the surface chemistry of carbon can increase its hydrophilic character.[24] As a consequence, it becomes wettable, and metal oxide dispersion is enhanced. Oxygen-enriched surfaces have been widely used in a variety of modification processes, including gaseous or aqueous oxidation, ozonation, and gamma irradiation, *etc.* Aqueous oxidation enhanced carboxylic acid functional groups significantly, whereas gaseous oxidation enhanced carbonyl and hydroxyl functional groups significantly. While ozonation increases the number of acid surface groups, it alters the surface area and porosity.[25]

In this study, porous carbon impregnated with iron oxide was utilized to fabricate a molecular sieve for CO_2/CH_4 separation. Palm kernel shell biomass was a precursor to porous carbon. Three different oxidation processes were evaluated in order to increase the hydrophilicity of carbon: oxidation with 10% H_2O_2, ozonation with distilled water, and ozonation with 10% H_2O_2 solution. In the CMS preparation, the oxidation processes are followed by iron oxide impregnation and calcination. An investigation of the effect of three different oxidation processes on the dispersion of iron oxide impregnated porous carbon on separation performance is conducted, which has not been previously described. In this study, the characterization of materials is extended to ensure the feasibility of impregnation, adsorption isotherms, and breakthrough separation for the purpose of separation.

2 Experimental

2.1. Materials

Porous carbon from palm kernel shell (20–25 mesh) was obtained from PT Home System Indonesia. Hydrogen peroxide with a purity of 50% from PT Indonesia Inti Pratama. Iron(III) nitrate nonahydrate for analysis EMSURE® ACS, ISO, Reag. Ph Eur from Merck. Nitrogen with a purity of 99.95% was used as inert gas in the calcination process. Methanol for analysis EMSURE® ACS, ISO, Reag. Ph Eur from Merck as a solvent for metal impregnation. CO_2 and CH_4 with a purity of 99.9% were obtained from PT. Aneka Gas Industri Indonesia as adsorbate. A mixed gas CH_4/CO_2 (55/45% v/v) as a biogas representative.

2.2. Preparation of oxidized carbon

Oxidized carbon was obtained by oxidizing porous carbon with H_2O_2 (10% v/v), ozonating it with distilled water, and ozonating it with an H_2O_2 (10% v/v) solution. To oxidize a porous carbon with a 10% H_2O_2 solution, a 15 g porous carbon was mixed with 150 mL 10% H_2O_2 solution at room temperature for two hours, followed by filtering and heating to 60 °C for 24 hours. As part of the ozonation process, a 1 : 10 (w/v) mixture of porous carbon and distilled water was placed in the ozone contact reactor (IONTECH QLA-3G ozone generator). Ozone gas was fed into the system at a flow rate of 3000 mg h^{-1} and a power output of 60 watts for 120 minutes. The ozone–H_2O_2 reaction was initiated by substituting distilled water for a 10% H_2O_2 solution.

2.3. Impregnation of iron oxide

The iron oxide was dispersed on porous carbon by an incipient wetness method, followed by calcination. At first, pristine 15 g carbon was degassed at a temperature of 150 °C for 2 hours in order to clean the pores. Carbon pores were then slowly filled with a salt solution of 5.4 g iron(III) nitrate nonahydrate in 12 mL methanol. The sample was heated under nitrogen flow for 6 hours at 500 °C during the calcination process. Iron as iron oxide was targeted at 5% by weight. The procedure was also applied to oxidized carbon. A schematic of the CMS preparation is presented in Fig. 1.

2.4. CMS characterization

Fourier transforms infrared (FTIR) analysis was carried out for the functional group's characterization of the material by using Nicolet Avatar 360 IR. In this study, samples were analyzed at a wavelength of 400–4000 cm^{-1}. The morphology of the CMSs was characterized by SEM-EDX instrument using JEOL JSM-6510 LA at a voltage of 10 kV. The structure of crystalline materials was characterized by XRD using Bruker D2 Phaser. The diffractogram was obtained by using Cu-K_α radiation (λ = 1.5406 Å) in the range $10° < 2\theta < 90°$.

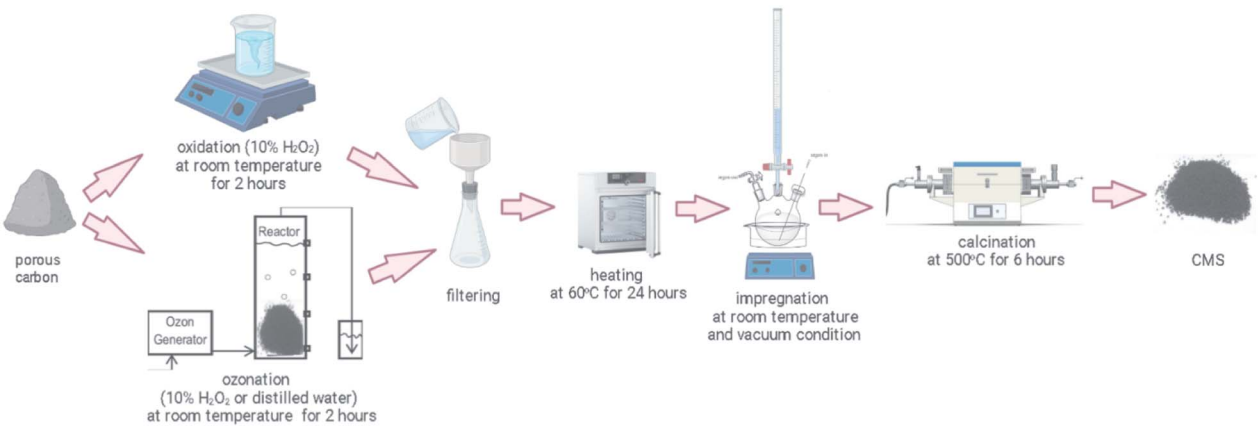

Fig. 1 Schematic procedure of iron oxide impregnation onto porous carbon as CMS.

2.5. Adsorption isotherm measurement

The adsorption capacity of CO_2 and CH_4 was measured by the volumetric method from 0 to 1.2 atm at a temperature of 30 °C. An ultrahigh vacuum adsorption apparatus rig was constructed using Swagelok® VCR valves and fittings. First, CMS samples were degassed for 6 hours at 150 degrees celsius until a static pressure of at least 0.01 torr was reached. These results are presented as an adsorption isotherm curve. The schematic diagram and procedure for measuring adsorption isotherms have been published in the literature.[26]

2.6. Separation performance with a breakthrough analysis

The composition of mixed gases (CH_4 and CO_2) was determined using a portable gas analyzer (Biogas Analyzer Gas Board 3200plus, Hubei Cubic-Ruiyi Instrument Co., Ltd.). The material was first placed in the column with fixed bed dimensions (D = 9.5 mm and L = 300 mm), followed by a 200 mL min^{-1} nitrogen flush until no gas content of CH_4, CO_2, or O_2 could be detected on the gas detector. The mixed gas mixture, comprised of CH_4 and CO_2, was then introduced into the system at a flow rate of 50 mL min^{-1} at room temperature and 1.2 bar pressure. The separation cycle was continued until the gas composition returned to the initial concentrations of the gas inlet.[13]

3 Results and discussion

3.1. CMS characteristics

Functional groups and surface morphologies. Fig. 2(a) illustrates the FT-IR spectra of CMSs. The spectral characteristics of pristine and oxidized carbon correspond to wavelengths of 3440 cm^{-1}, 2350 cm^{-1}, 1580 cm^{-1}, 1130 cm^{-1}. The peak of 3440 cm^{-1} represents the presence of a hydroxyl group (O–H stretching).[27] Meanwhile, the peak of 1580 cm^{-1} and 1130 cm^{-1} denote the presence of a carboxyl group (C=O stretching)[27–30] and C–O group (stretching), respectively.[29] It is remarkable that there is an increase in the intensity of the O–H stretching, C=O stretching, and C–H stretching when compared to pristine carbon. As a result, the oxygen groups on all oxidized carbons increase.

As shown in Fig. 2(b), the FTIR spectrum and absorption bands of iron oxide impregnated porous carbon. There is an addition at the peak of 590 cm^{-1} in comparison to the pristine and oxidized carbon prior to iron oxide impregnation. This peak is thought to be caused by Fe–O bonds. A peak at 576.3 cm^{-1} was also observed in a composite of activated carbon and iron oxide (Fe_3O_4).[31]

SEM images of each material reveal the oxidized carbon's morphological structure (CH, COA, and COH). Fig. 3 illustrates the results of SEM images of C (a), CH (b), COA (c), and COH.

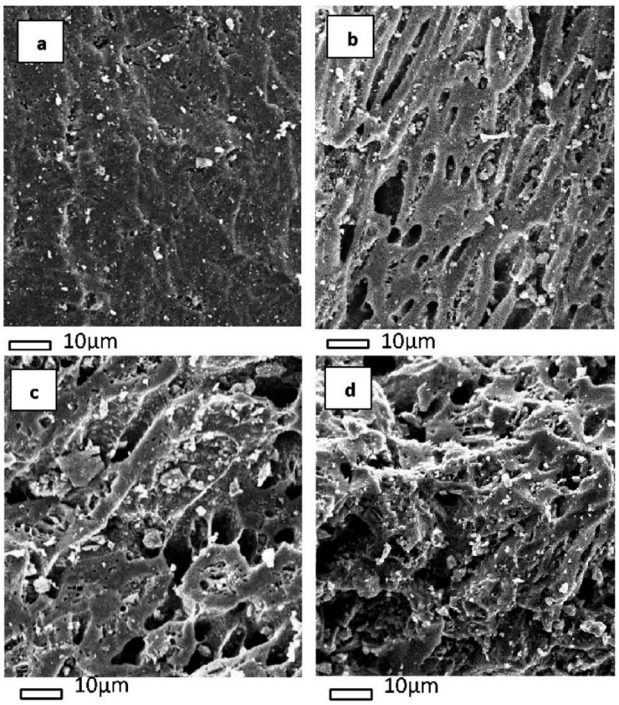

Fig. 3 SEM images of (a) C, (b) CH, (c) COA, and (d) COH.

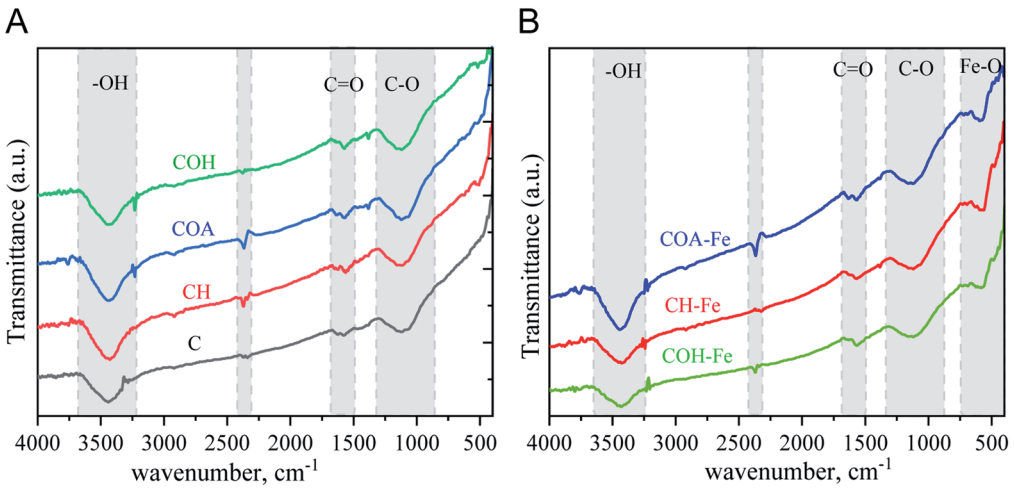

Fig. 2 FT-IR spectra of (A) oxidized carbon, and (B) oxidized carbon impregnated with iron oxide.

Table 1 Percentage increase in oxygen groups for CH, COA and CH

Oxidation method	Sample	Element (%)		Addition of oxygen group (%)
		C	O	
Pristine carbon	C	93.06	6.94	—
Oxidation using 10% H_2O_2 solution	CH	91.07	8.93	28.67
Ozonation using distilled water	COA	87.77	12.33	79.74
Ozonation using 10% H_2O_2 solution	COH	89.95	10.05	38.43

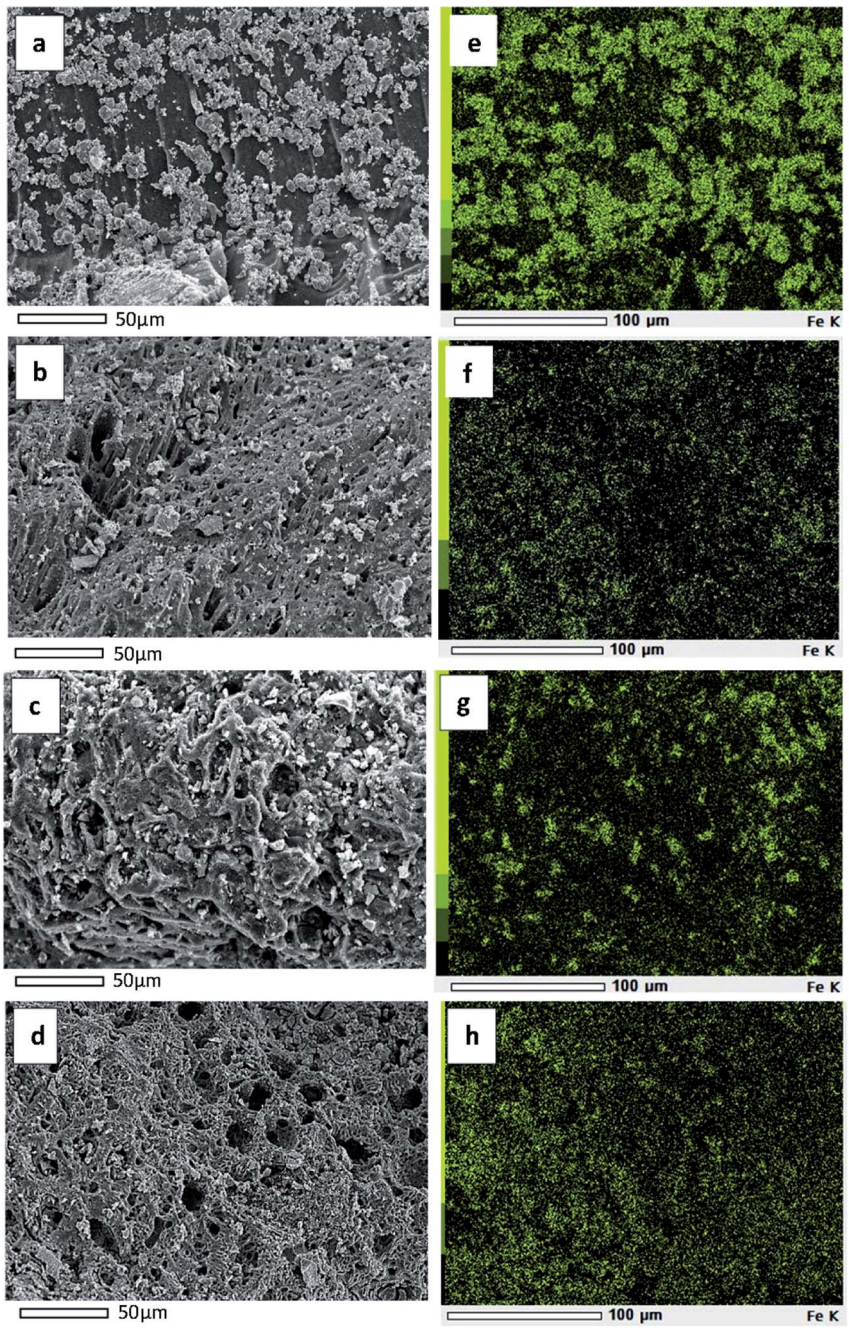

Fig. 4 SEM images of C–Fe (a), CH–Fe (b), COA–Fe (c), COH–Fe (d) and their elemental mapping of Fe on C–Fe (e), CH–Fe (f), COA–Fe (g), COH–Fe (h).

Table 2 Elements detected on CMSs by EDX analysis

	Element (%)		
Sample	C	O	Fe
C–Fe	83.47	10.57	5.96
CH–Fe	80.97	13.78	5.25
COA–Fe	73.23	20.96	5.81
COH–Fe	79.71	14.79	5.50

SEM images reveal an increase in the size of oxidized carbon pores.[25] This increase has been modified by either oxidation treatment using 10% H_2O_2 solution, ozonation using distilled water, or ozonation using 10% H_2O_2 solution. According to the SEM images, the pore size of the carbon can become irregular as a result of the ozonation process, whether using distilled water (COA) or a 10% H_2O_2 solution. In comparison to carbon, which is oxidized with a 10% H_2O_2 solution (CH). Despite the increased size of the CH pore cavities, the carbon structure remains regular.

The composition of C and O was determined *via* SEM-EDX analysis. Table 1 summarizes the percentage increase in oxygen groups for CH, COA, and CH. It can be concluded that each treatment increases the oxygen groups in the following order: COA > COH > CH.

The SEM micrographs of C–Fe (a), CH–Fe (b), COA–Fe (c), and COH–Fe (d), as well as the elemental mapping of iron oxide on C–Fe (e), CH–Fe (f), COA–Fe (g), and COH–Fe (h), are shown in Fig. 4. Based on Fig. 4(a–d), it can be seen that there are some small aggregates of iron oxide visible from the lateral view of the CMS. These aggregates are brighter in colour and are supported on the darker surface of the porous carbon.

As shown in Fig. 4(a) and its elemental mapping in Fig. 4(e), an agglomeration of iron oxide exists on the pristine carbon surface. This demonstrates that the iron salt solution is incapable of spreading uniformly across the pristine carbon surface, resulting in the formation of iron oxide agglomerates. This is because the iron salt solution is unable to wet the surface of the pristine carbon due to its hydrophobic nature. While iron oxide is widely dispersed on the surface of oxidized carbon, as illustrated in Fig. 4(b–d) and as indicated by the elemental mapping in Fig. 4(f–h). This indicates that the addition of oxygen functional groups increases the wettability of carbon while decreasing its hydrophobicity. The composition of iron oxide impregnated porous carbon was determined *via* SEM-EDX analysis. The results are presented in Table 2.

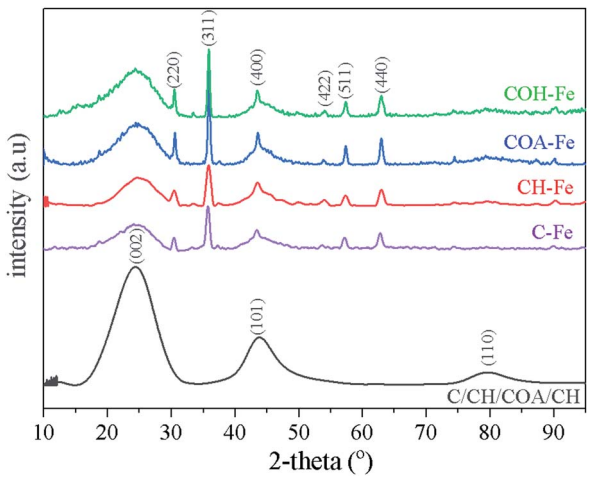

Fig. 5 XRD pattern of CMSs.

Crystallinity of CMSs. The crystal structure of iron oxide on porous carbon can be determined using X-ray diffraction patterns. Fig. 5 illustrates the XRD patterns of porous carbon and iron oxide impregnated carbon. Amorphous carbon is indicated by the diffraction peaks of pristine and oxidized carbon in the planes of (002), (101), and (110) indicate the amorphous carbon. Meanwhile, for all oxidized carbon, the diffraction peaks at 2θ value of 30.5°, 35.9°, 43.5°, 54.0°, 57.2°, and 63° indicate the presence of Fe_3O_4 in the cubic spinel structure of (220), (311), (400), (422), (511), and (440) confirmed.[32] Thus, the iron oxides prepared are magnetite. From the diffraction peak obtained, no other phase of iron oxide is detected in the sample.

An estimation of the magnetite Fe_3O_4 crystallite size was performed using Debye–Scherrer's equation. The mean crystallite size calculated from the main diffraction peak (311) around 35.9° was listed in Table 3.

Nitrogen sorption analysis. The textural properties were determined using N_2 adsorption–desorption analysis. Fig. 6 illustrates the results. According to the IUPAC classification, both pristine and oxidized carbon exhibit a type I isotherm, which is characteristic of microporous materials. Pristine carbon has a large amount of nitrogen adsorbed (*ca.* 225 cm^3 g^{-1} STP at $1P/P_0$). The volume of nitrogen adsorbed by oxidized carbon decreases. Interestingly, the isotherm of adsorption–desorption for oxidized carbon is not closed. This is most likely due to the presence of pores in the shape of an ink bottle following the oxidation process.[13] The pore size distribution was evaluated using the Horvath–Kawazoe (HK) model. Pristine carbon-centered at 0.75 nm. These findings establish unequivocally that pristine carbon exists in a microporous region. Due to the formation of cavities during oxidation, the center of oxidized carbon shifts to a larger size of approximately 0.8–1 nm.[25]

Fig. 6(b) shows a nitrogen sorption isotherm for oxidized carbon impregnated with iron oxide. As can be seen from the isotherm, the CMS also has a type I isotherm. Interestingly,

Table 3 Crystallite size of Fe_3O_4 for all oxidized carbon from Scherrer's equation calculation

Sample	Crystallite size, nm
C–Fe	18.34
CH–Fe	9.65
COA–Fe	16.93
COH–Fe	14.57

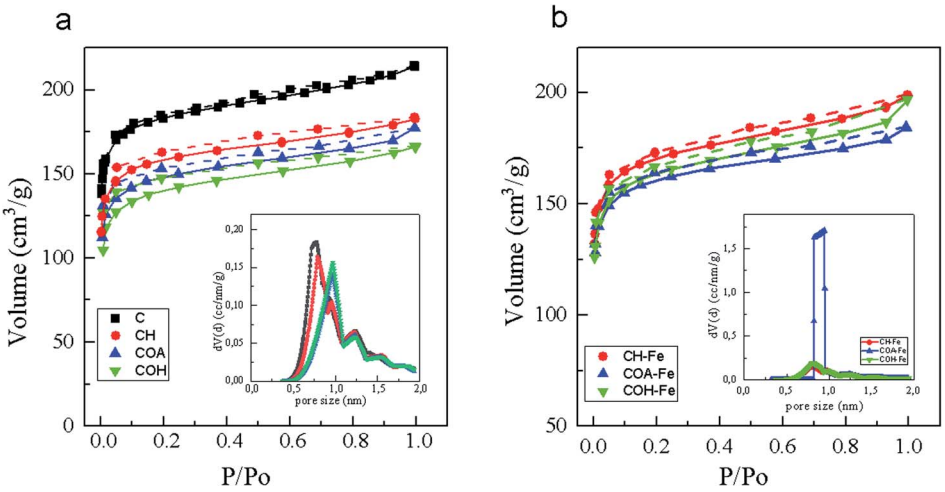

Fig. 6 Nitrogen adsorption–desorption isotherm for oxidized carbon (a) and iron oxide impregnated carbon (b) (inset: pore size distribution). Unit *y*-axis is in Standard Temperature and Pressure (STP).

Table 4 Pore textural properties evaluated by nitrogen sorption

Parameter	C	CH	COA	COH	CH–Fe	COA–Fe	COH–Fe
SSA, $m^2\ g^{-1}$	708	602	561	528	649	612	622
S_{mic}, $m^2\ g^{-1}$	651	560	520	491	603	573	573
% S_{mic}	92.0	93.0	92.7	93.0	93.0	93.6	92.1
V, $cm^3\ g^{-1}$	0.33	0.28	0.27	0.26	0.31	0.29	0.30
V_{mic}, $cm^3\ g^{-1}$	0.25	0.22	0.21	0.20	0.23	0.22	0.22
% V_{mic}	75.8	78.6	77.8	76.9	74.2	75.9	73.3
D_{avg}, nm	1.88	1.90	1.95	1.96	1.89	1.86	1.95

COA–Fe has a narrow and sharp pore size distribution compared to other materials, which is advantageous for CMS applications.

Table 4 summarizes the specific surface area (SSA), micropore surface area (S_{mic}), total pore volume (V), micropore volume (V_{mic}), and mean pore diameter (D_{avg}). Pristine carbon has a high surface area of 708 $m^2\ g^{-1}$, but its specific surface area decreases by *ca.* 15–25% after oxidation and iron oxide loading. The reduction is most likely the result of cavities formed during the oxidation process[33] and the pore being occupied during the impregnation process.[13,21,34] All materials exhibit a predominance of microporous structure, both in terms of surface area and pore volume.

3.2. CO_2 and CH_4 adsorption isotherm

The CO_2 and CH_4 adsorption isotherm curves in. Fig. 7(a) were determined at a temperature of 30 °C and pressure of up to 1 atm. As shown in Fig. 7(a), the CO_2 uptake capacity was significantly greater than the CH_4 uptake capacity. It was consistent with the other outcomes.[13] Furthermore, impregnation with iron oxide can increase CO_2 uptake capacity while decreasing CH_4 uptake capacity. The uptake capacity of CH_4 on the impregnated carbon is lower than that of pristine carbon. The increased capacity for CO_2 uptake is most likely due to the iron oxide, as the active site has a higher affinity for CO_2 than the pristine carbon surface. However, impregnation of carbon with iron oxide resulted in a decrease in the affinity of CH_4. It will improve CO_2/CH_4 selectivity, which is beneficial for CO_2/

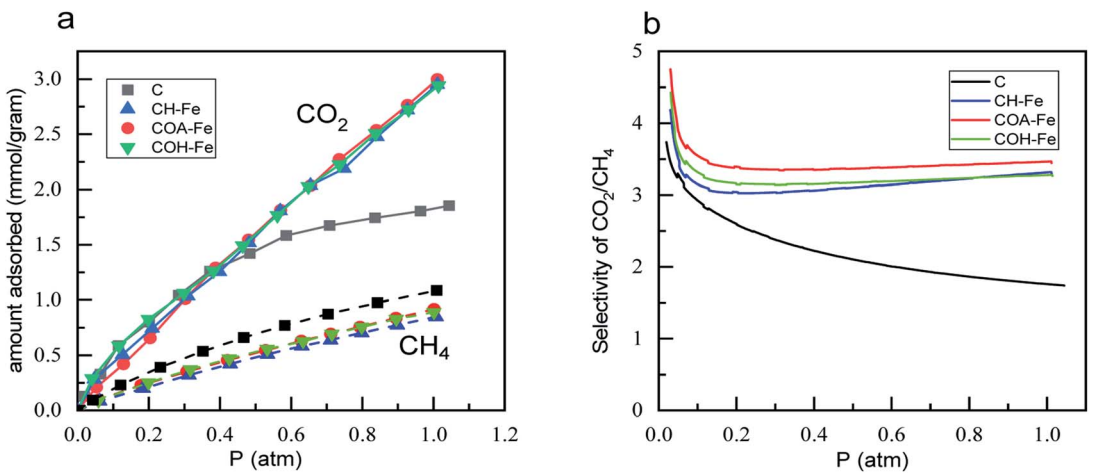

Fig. 7 Adsorption of CO_2 and CH_4 on pristine carbon, CH–Fe, COA–Fe and COH–Fe (a) and selectivity of CO_2/CH_4 (b) at temperature of 30 °C.

Table 5 Comparison of adsorption capacity with other investigations at various temperatures and the pressure of 1 bar

Sorbent type	Metal/metal oxide	Uptake capacity of CO_2, mmol g^{-1}	Temp., °C	Ref.
Oxidized AC (CH)	Fe_3O_4	2.95	30	This work
Oxidized AC (COA)	Fe_3O_4	3.01	30	This work
Oxidized AC (COH)	Fe_3O_4	2.94	30	This work
Mesoporous carbon	NiO	2.00	30	37
AC	MgO	2.72	0	38
AC	Cu/Zn	2.25	30	39
AC	CuO	0.30	25	40
Unmodified AC	NiO	3.02	30	41

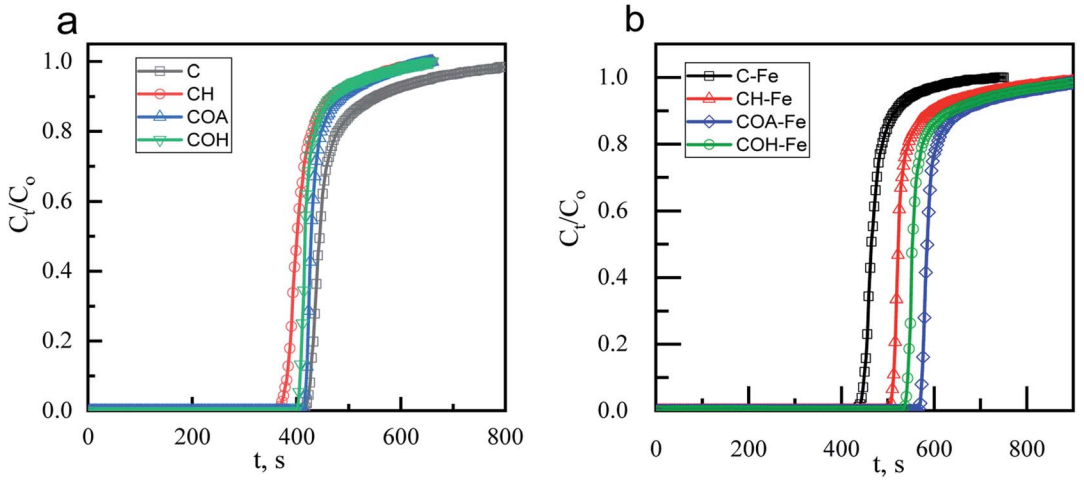

Fig. 8 Carbon dioxide-breakthrough curves of mixed gas CO_2/CH_4 for (a) C, CH, COA and COH; (b) C–Fe, CH–Fe, COA–Fe and COH–Fe.

CH_4 separation. The pristine carbon has a CO_2 uptake capacity of 1.85 mmol g^{-1} at a pressure of 1 bar, whereas the CH–Fe, COA–Fe, and COH–Fe have capacities of 2.94 mmol g^{-1}, 3.00 mmol g^{-1}, and 2.94 mmol g^{-1}, respectively. Meanwhile, the CH_4 uptake capacities of pristine carbon, CH–Fe, COA–Fe, and COH–Fe are respectively 1.08 mmol g^{-1}, 0.85 mmol g^{-1}, 0.92 mmol g^{-1}, and 0.89 mmol g^{-1}. In comparison to other studies in the literature (Table 5), the CO_2 uptake capacity of oxidized carbon impregnated with iron oxide is attractive and can compete with other impregnation of metal oxide.

The selectivity of CO_2/CH_4 is a critical factor in the separation of CO_2/CH_4. Fig. 7(b) illustrates the selectivity of CO_2/CH_4. The data indicate that as pressure increases, the selectivity value of pristine carbon decreases, which is consistent with previous literature.[13,35] On the pressure range investigated, the selectivity of CO_2/CH_4 for pristine carbon was *ca.* 3.75–1.7. Interestingly, for iron oxide-impregnated carbon, the selectivity increased as the pressure was increased. This is most likely because CO_2 chemisorption occurs at active sites such as iron oxide. Iron oxide's active sites may have a strong affinity for CO_2. As a result, the intermolecular interaction between CO_2 and iron oxide is much stronger than the interaction between CH_4 and iron oxide, resulting in a significant increase in the uptake capacity

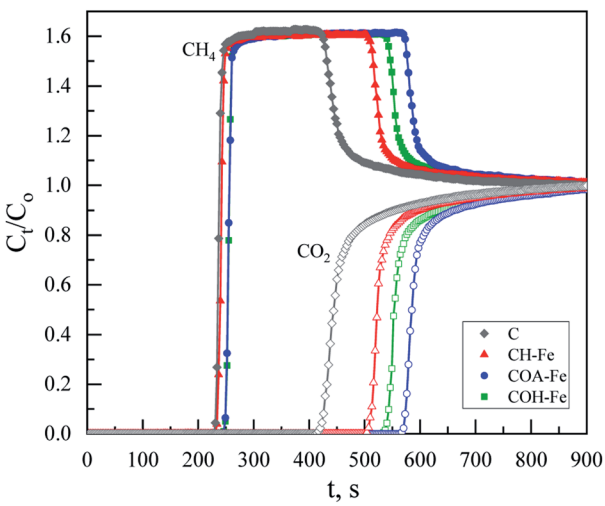

Fig. 9 Breakthrough curves of mixed gas CO_2/CH_4 (◆C, ▲CH–Fe, ●COA–Fe, ■COH–Fe for CO_2 and ◇C, ΔCH–Fe, □COA–Fe, ○COA–Fe for CH_4).

of CO_2 as the gas's pressure increases. As a result, CO_2 has a greater selectivity than CH_4.[36] Meanwhile, physisorption occurs as a result of CO_2 adsorption onto pristine carbon. When

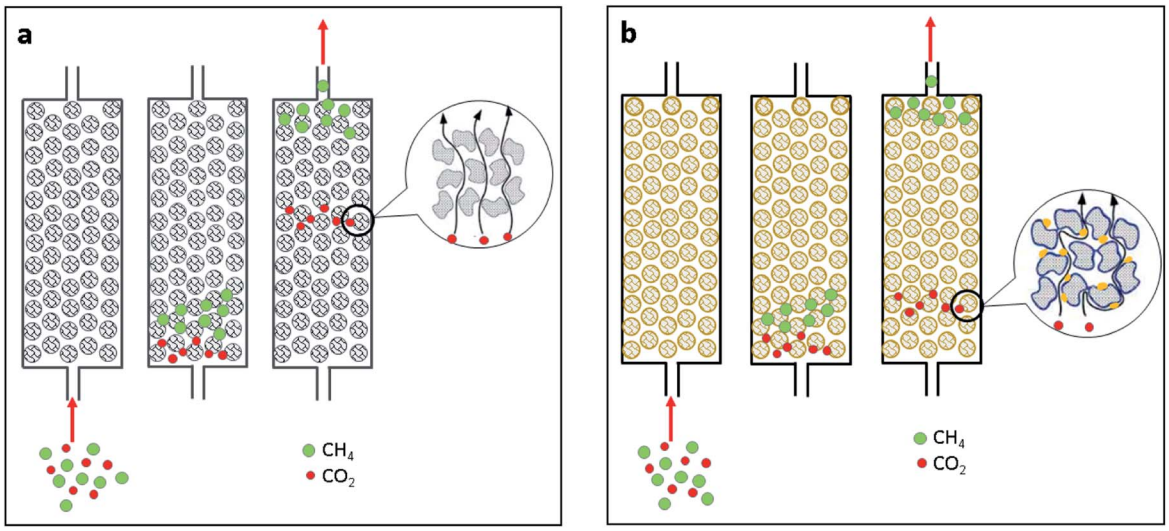

Fig. 10 Separation mechanism using (a) pristine carbon and (b) oxidized carbon impregnated with iron oxide.

iron oxide impregnated oxidized carbon was compared to pristine carbon, the selectivity of CO_2/CH_4 increased up to 190%.

3.3. Performance of CO_2/CH_4 separation

The breakthrough analysis was conducted to determine the CO_2/CH_4 separation performance of the materials. A 45 : 55% mixture of CO_2/CH_4 was flowed into a packed bed column containing the material, and the gas composition at the outlet was monitored over time. The CO_2 breakthrough curve is depicted in Fig. 8. The breakthrough curves plot the outlet concentration of gas species at a certain time (C_t)/the initial inlet concentration (C_0) *versus* time. As illustrated in Fig. 8(a), there was no difference in the time required to achieve CO_2 breakthrough between pristine and oxidized carbon. Thus, oxidation enhances the oxygen functional group on the carbon surface but does not transform the time of the breakthrough. Based on the data, iron oxide impregnated-oxidized carbon has an increase in CO_2 breakthrough time (see Fig. 8(b)). Pristine carbon achieved a CO_2 breakthrough time of 400 s, while iron oxide impregnated-pristine carbon increased slightly (425 s). However, iron oxide impregnated-oxidized carbon resulted in a 25–45% increase. The breakthrough time for CO_2 was defined as when the concentration of CO_2 reaches 5%, whereas the requirement for biomethane is at least 95%. CH–Fe, COA–Fe, and CH–Fe had CO_2 breakthrough times of 500 s, 570 s, and 530 s, respectively. The CO_2 breakthrough curve may indicate that iron oxide impregnated oxidized carbon prepared *via* ozonation with distilled water has a superior iron oxide dispersion. The order of the CO_2 breakthrough time is CH–Fe < COH–Fe < COA–Fe. The results of this study indicate that the addition of oxygen groups to carbon surfaces can increase iron oxide dispersion on the surface, which can enhance CO_2/CH_4 separation.

Fig. 9 displays the breakthrough curves of CO_2 and CH_4 for the materials. As shown in Fig. 9, no CH_4 or CO_2 gas is present initially until approximately 250 seconds, after which CH_4 appears with a purity of >98 percent until a certain time, and finally, CO_2 emerges until the final concentration in the outlet equals the inlet. A similar CH_4 breakthrough time was obtained for all materials, but with a different CO_2 breakthrough time. A delayed flow of CH_4 at the outlet could indicate a slower diffusion of gas through the bed, caused by the interaction of carbon surface with gas species. Additionally, a larger curve between the CH_4 and CO_2 signals indicated that CO_2 and CH_4 had a better separation performance. COA–Fe generates the largest curve.

Generally, the separation process resembles that of chromatographic separation. The chromatography separation occurs when the components with a faster rate of movement are separated first. In the separation of CO_2/CH_4, molecule types with higher diffusivity values or those that diffuse more rapidly are separated first. The illustration mechanism of separation is depicted in Fig. 10. In a column, as shown in Fig. 10(a) and (b), CH_4 diffuses more rapidly than CO_2.[13] Therefore, CH_4 and CO_2 can be separated. CO_2 diffuses more slowly over iron oxide impregnated carbon in Fig. 10(b) than it does over pristine carbon (Fig. 10(a)). Iron oxide exhibits a stronger affinity for CO_2. This can result in increased interaction between CO_2 and the iron oxide active surface, resulting in a slower rate of CO_2 diffusion in the CMS column. As a result, the process of separation lengthens.

3.4. Performance comparison on CH–Fe_2O_3 and CH–Fe_3O_4

The type of iron oxide formed in this study is Fe_3O_4. CH–Fe_3O_4 was mentioned previously in conjunction with CH–Fe, which can improve CO_2/CH_4 separation performance by up to 125%. Its performance will be compared to that of other types of iron oxide. Hematite (Fe_2O_3) was chosen as a representative of other iron oxides due to its high affinity for CO_2.[20] Fig. 11 compares the CO_2 breakthrough for CH, CH–Fe_3O_4, and CH–Fe_2O_3. The CO_2 breakthrough curves for all samples are ideal, indicating

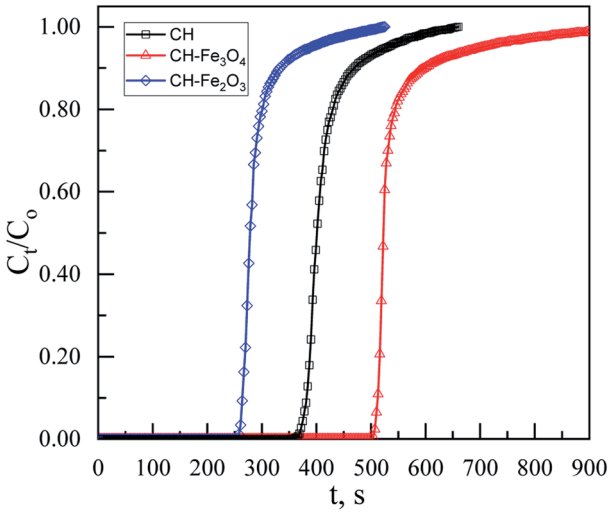

Fig. 11 Carbon dioxide-breakthrough curves of mixed gas CO_2/CH_4 for CH, CH–Fe_3O_4, and CH–Fe_2O_3.

that mass transfer occurs instantaneously.[13] The order of breakthrough time is CH–Fe_2O_3 (260 s) < CH (400 s) CH–Fe_3O_4 (500 s).

4 Conclusions

The feasibility of preparing iron oxide impregnated porous carbon was investigated. In this study, increased dispersion of iron oxide on the carbon surface can be achieved by adding oxygen *via* the three oxidation processes used. The impregnation of iron oxide on oxidized carbon can be characterized as CMS for CO_2/CH_4 separation. CMS, which was obtained by aqueous ozonation with distilled water, followed by impregnation with iron oxide and labeled COA–Fe, exhibited superiority. The COA–Fe can provide an enhancement of CO_2 uptake capacity up to *ca.* 1.7 times at 30 °C and 1 atm, while the enhancement of CO_2/CH_4 separation up to *ca.* 45% compared to pristine carbon. Furthermore, the iron oxide of Fe_3O_4 is more favorable for CO_2/CH_4 separation than that of Fe_2O_3.

Author contributions

Nur Indah Fajar Mukti: conceptualization, investigation, methodology, formal analysis, funding acquisition, writing-original draft. Teguh Ariyanto: supervision, funding acquisition, writing-review and editing. Wahyudi Budi Sediawan: supervision, writing-review and editing. Imam Prasetyo: conceptualization, supervision, funding acquisition, writing-review and editing.

Conflicts of interest

There are no conflicts to declare.

Acknowledgements

This research was supported by Indonesia Endowment Fund for Education (LPDP), Indonesian Ministry of Finance through Dissertation Research Grant (Beasiswa BUDI-DN). The authors wish thanks to PT Home System for the gift of porous carbon produced from palm kernel shell.

References

1 I. U. Khan, M. H. D. Othman, H. Hashim, T. Matsuura, A. F. Ismail, M. Rezaei-DashtArzhandi and I. W. Azelee, *Energy Convers. Manage.*, 2017, **150**, 277–294.
2 I. Angelidaki, L. Treu, P. Tsapekos, G. Luo, S. Campanaro, H. Wenzel and P. G. Kougias, *Biotechnol. Adv.*, 2018, **36**, 452–466.
3 M. T. Kallo and M. J. Lennox, *Langmuir*, 2020, **36**, 13591–13600.
4 O. W. Awe, Y. Zhao, A. Nzihou, D. P. Minh and N. Lyczko, *Waste Biomass Valorization*, 2017, **8**, 267–283.
5 X. Y. Chen, H. Vinh-Thang, A. A. Ramirez, D. Rodrigue and S. Kaliaguine, *RSC Adv.*, 2015, **5**, 24399–24448.
6 I. Durán, N. Álvarez-Gutiérrez, F. Rubiera and C. Pevida, *Chem. Eng. J.*, 2018, **353**, 197–207.
7 I. Prasetyo, R. Rochmadi and E. Wahyono, *Reaktor*, 2010, **13**, 24–30.
8 N. K. Jensen, T. E. Rufford, G. Watson, D. K. Zhang, K. I. Chan and E. F. May, *J. Chem. Eng. Data*, 2012, **57**, 106–113.
9 M. Younas, M. Sohail, L. L. Kong, M. J. K. Bashir and S. Sethupathi, *Int. J. Environ. Sci. Technol.*, 2016, **13**, 1839–1860.
10 I. Prasetyo, N. I. F. Mukti, R. B. Cahyono, A. Prasetya and T. Ariyanto, *Waste Biomass Valorization*, 2020, **11**, 5599–5606.
11 I. Prasetyo and D. D. Do, *Chem. Eng. Sci.*, 1998, **53**, 3459–3467.
12 I. Prasetyo, R. Rochmadi, E. Wahyono and T. Ariyanto, *Eng. J.*, 2017, **21**, 83–94.
13 T. Ariyanto, K. Masruroh, G. Yunita, S. Pambayun, N. Indah, F. Mukti, R. B. Cahyono, A. Prasetya and I. Prasetyo, *ACS Omega*, 2021, **6**, 19194–19201.
14 W. Lou, J. Yang, L. Li and J. Li, *J. Solid State Chem.*, 2014, **213**, 224–228.
15 D. Britt, H. Furukawa, B. Wang, T. G. Glover and O. M. Yaghi, *Proc. Natl. Acad. Sci. U. S. A.*, 2009, **106**, 20637–20640.
16 J. Alcañiz-Monge, J. P. Marco-Lozar and D. Lozano-Castelló, *Fuel Process. Technol.*, 2012, **95**, 67–72.
17 Z. Yang, D. Wang, Z. Meng and Y. Li, *Sep. Purif. Technol.*, 2019, **218**, 130–137.
18 A. R. Mohamed, M. Mohammadi and G. N. Darzi, *Renew. Sustain. Energy Rev.*, 2010, **14**, 1591–1599.
19 S. J. Kim, Y. Kwon, D. Kim, H. Park, Y. H. Cho, S. E. Nam and Y. I. Park, *Membranes*, 2021, **11**(482), 1–34.
20 A. Hakim, T. S. Marliza, N. M. Abu Tahari, R. W. N. W. Isahak, R. M. Yusop, W. M. Mohamed Hisham and A. M. Yarmo, *Ind. Eng. Chem. Res.*, 2016, **55**, 7888–7897.

21 B. G. H. Briton, L. Duclaux, Y. Richardson, K. B. Yao, L. Reinert and Y. Soneda, *Appl. Water Sci.*, 2019, **9**, 1–14.
22 J. G. Mahy, L. Tasseroul, A. Zubiaur, J. Geens, M. Brisbois, M. Herlitschke, R. Hermann, B. Heinrichs and S. D. Lambert, *Microporous Mesoporous Mater.*, 2014, **197**, 164–173.
23 I. Mazilu, C. Ciotonea, A. Chirieac, B. Dragoi, C. Catrinescu, A. Ungureanu, S. Petit, S. Royer and E. Dumitriu, *Microporous Mesoporous Mater.*, 2017, **241**, 326–337.
24 A. Barroso-Bogeat, M. Alexandre-Franco, C. Fernández-González and V. Gómez-Serrano, *Arab. J. Chem.*, 2019, **12**, 3963–3976.
25 A. Annisa, I. Prasetyo, D. Swantomo and T. Ariyanto, *4th Int. Semin. Chem.*, 2021, 2349, p. 020007.
26 I. Prasetyo, N. I. F. Mukti, M. Fahrurrozi and T. Ariyanto, *ASEAN J. Chem. Eng.*, 2018, **18**, 09–16.
27 B. Lesiak, N. Rangam, P. Jiricek, I. Gordeev, J. Tóth, L. Kövér, M. Mohai and P. Borowicz, *Front. Chem.*, 2019, **7**(642), 1–16.
28 V. Tucureanu, M. Alina and M. A. Andrei, *Crit. Rev. Anal. Chem.*, 2016, **46**, 502–520.
29 W. Yang, Z. Du, Z. Ma, G. Wang, H. Bai and G. Shao, *RSC Adv.*, 2016, **6**, 3942–3950.
30 J. L. Figueiredo, M. F. R. Pereira, M. M. A. Freitas and J. J. M. Órfão, *Carbon*, 1999, **37**, 1379–1389.
31 P. L. Hariani, M. Faizal, R. Ridwan, M. Marsi and D. Setiabudidaya, *Sustain. Environ. Res.*, 2018, **28**, 158–164.
32 S. Kamilah, C. Soh, A. Azzura, A. Rahman and M. Shamsuddin, *Malaysian J. Anal. Sci.*, 2018, **22**, 768–774.
33 G. Lota, P. Krawczyk, K. Lota and A. Sierczy, *J. Solid State Electrochem.*, 2016, **20**, 2857–2864.
34 S. H. Khalil, M. K. Aroua and W. M. A. W. Daud, *Chem. Eng. J.*, 2012, **183**, 15–20.
35 W. Liang, Z. Liu, J. Peng, X. Zhou, X. Wang and Z. Li, *Energy Fuels*, 2019, **33**, 493–502.
36 M. Bokare, S. Bano, P. S. Antony, S. Pal and R. Biniwale, *Adsorption*, 2020, **26**, 51–59.
37 J. A. Schott, Z. Wu, S. Dai, M. Li, K. Huang and J. A. Schott, *Microporous Mesoporous Mater.*, 2017, **249**, 34–41.
38 S. Shahkarami, A. K. Dalai and J. Soltan, *Ind. Eng. Chem. Res.*, 2016, **55**, 5955–5964.
39 S. Hosseini, I. Bayesti, E. Marahel and F. Eghbali, *J. Taiwan Inst. Chem. Eng.*, 2015, 1–9.
40 B. Kim, K. Cho and S. Park, *J. Colloid Interface Sci.*, 2010, **342**, 575–578.
41 D. Jang and S. Park, *Fuel*, 2012, **102**, 439–444.